

Full length article

## Exploring the structure and electronic properties of individual hybrid GO/rGO flakes

M. Navarro-Rodriguez <sup>a</sup>, V. Camús <sup>b</sup>, A. Cros <sup>b</sup>, N. Garro <sup>b</sup>, Andres M. Somoza <sup>a</sup>,  
E. Palacios-Lidon <sup>a,\*</sup>

<sup>a</sup> University of Murcia, Centro de Investigación en Óptica y Nanofísica (CIOyN), Murcia, 30100, Murcia, Spain

<sup>b</sup> Universitat de València, Institut de Ciència dels Materials (ICMUV), Paterna, 46980, València, Spain



### ARTICLE INFO

#### Keywords:

Graphene oxide  
Reduced graphene oxide  
Kelvin probe force microscopy  
Raman spectroscopy  
Nanoscale conductivity

### ABSTRACT

Despite its great potential, the use of graphene oxide (GO) in sensors, photocatalysis, or biomedicine applications is limited by its low conductivity. This drawback is typically overcome by using its reduced form (rGO) albeit sacrificing some of its extensive chemical properties. In this study, we unveil a non-uniform reduction process that enables the fabrication of hybrid flakes consisting of both size tunable GO and rGO regions. The nanoscale resolution of Kelvin probe force microscopy together with co-localized Raman spectroscopy allow us to correlate the local reduction degree with the nanoscale electronic properties, chemical composition, and structural defects. Additionally, we introduce a reliable metric for quantifying the extent of reduction. This research opens up possibilities for the development of new 2D nanohybrid materials that combine the high reactivity of GO and the enhanced conductivity of rGO, enabling applications in selective functionalization.

### 1. Introduction

Graphene oxide (GO) and its reduced counterpart (rGO) were primarily viewed as a means of mass-producing graphene, but over the last decade they have found their own value as 2D materials. GO consists of a defective carbon basal plane randomly decorated with oxygen-containing functional groups [1–3]. These functional groups can be removed to produce rGO, drastically changing the electrical and chemical properties of the material. While GO is highly insulating, hydrophilic, and easily soluble in polar solvents, rGO is a good electrical conductor, hydrophobic, and insoluble in polar solvents. Despite the widely different properties of the two materials, the transition between GO and rGO is not sharp. Thus GO and rGO should be seen as the limiting cases of a family of closely related materials whose properties can be finely tuned and tailored for different purposes. This versatility, coupled with an easy production and processability [4–7] has allowed GO and rGO to find uses in a number of applications [8], such as the fabrication of opto-electronic devices and printed electrodes [9–11], catalysis [12–14], humidity sensors [15,16], biomedical applications [17–19] or water treatment [20].

During the preparation of GO, the oxygen-containing functional groups locally modify the  $sp^2$  hybridization in favor of  $sp^3$  [21]. This process disrupts the hexagonal lattice due to the addition of point

defects and vacancies, thus making GO highly disordered and non-stoichiometric. As the reduction process takes place, the  $sp^2$  hybridization is partially recovered, increasing the conductivity of the material up to several orders of magnitude [22–24]. The reduction degree is usually characterized by either the C/O ratio or the ratio of  $sp^2$  and  $sp^3$  bonds [21]. Typically, C/O ratios between 1.5 and 2.5 are attributed to GO, while C/O ratios above 8 are considered for rGO [24]. Raman scattering, which has been validated as one of the primary characterization techniques for graphene, could be a good tool for quantifying the reduction degree. Initial results rapidly evidenced a rather complicated scenario with the presence of additional spectral bands convoluted with the characteristic G and D peaks of graphene [25]. As established by Claramunt et al. [26], a Raman metric for GO and its derivatives should be based on five different peaks for first order scattering: G and D bands, and three additional peaks, D\*, D', and D', which have been related to chemical and structural disorder [26]. Despite these progresses, the correlation between the spectral parameters and the degree of reduction is not totally conclusive. Different approaches to monitor the oxygen content, either via the frequency shift of some bands [26], or employing intensity ratios of first [27] or second order features [28] have only achieved partial success. The strong dependence of the Raman peaks on the reduction procedure, whether thermal, chemical or

\* Corresponding author.

E-mail address: [elisapl@um.es](mailto:elisapl@um.es) (E. Palacios-Lidon).

by laser illumination, or even on the nature of the substrate [29] have so far prevented GO and rGO from having a universal Raman metric.

These techniques provide valuable information about the chemistry and structure of the materials. Nevertheless, this is not sufficient to fully predict their electrical properties. Conductivity in GO and rGO is not solely determined by the  $sp^2/sp^3$  ratio but rather by a combination of several factors like the local distribution of  $sp^2$  and  $sp^3$  regions, possible doping during the reduction process, the degree of graphitization of the underlying carbon lattice [21,30], or the amount of morphological defects. For this reason, the conductivity of the material is closely tied to the level of oxidation of the GO precursor, the reduction method, and the temperature at which the process is carried out.

Two main approaches are usually considered to obtain rGO: (i) thermal decomposition by heating the GO sheets in an inert atmosphere or in solution, and (ii) chemical reduction. For thermal decomposition, temperatures above 500 °C are needed to remove most attached molecules [30]. This process generates additional point defects and carbon vacancies due to the production of CO and CO<sub>2</sub>, thus making it unsuitable for the production of highly conducting, low-defect rGO. Chemical reduction is performed by using reducing agents such as hydrazine, sodium borohydride or ascorbic acid [24,31–33]. With this method, the sheets might undergo doping processes, and different functional groups are preferentially removed depending on the reducing agent. Chemical reduction followed by a thermal annealing to restructure the carbon lattice (above 700 °C) is commonly used for the production of highly conductive rGO [30].

Although significant effort has been made towards the characterization of the reduction process of GO, its correlation with the electronic properties of the resulting material is not clear. Macroscale analyses of the reduction process provide averaged information of the overall state of the material, but do not grant information at the submicrometer scale at which many relevant charge transport processes take place. In recent years, a significant number of studies have been conducted to gain a deeper understanding of the transition from GO to rGO at the nanoscale. These studies aim to uncover the impact of various parameters in the reduction process, as well as to modify or determine the evolution of the local properties over individual sheets or thin films. Transmission Electron Microscopy (TEM) and Atomic Force Microscopy (AFM) have proved to be very valuable tools. In situ reduction studies performed with TEM have shown the structural evolution of GO during thermal decomposition [34,35], and correlated conductivity measurements with the structural evolution throughout the reduction process [36]. The versatility of AFM can be exploited twofold. In the first place, AFM can actively modify the flakes and create nanoscale conductive pathways through local reduction of the GO sheets [37–39]. Secondly, the evolution of the electrostatic properties can be monitored through different scanning probe techniques: Scanning Polarization Force Microscopy (SPFM) and Electrostatic Force Microscopy (EFM) [40–43], conductive AFM (c-AFM) [44], and Kelvin Probe Force Microscopy (KPFM) [45,46].

In this work we study the transition from GO to rGO through hydrazine chemical reduction at the nanoscale, focusing on individual monolayer flakes. We have characterized the intermediate states and monitored the evolution of the chemical and electronic properties during the reduction process by using Kelvin Probe Force Microscopy (KPFM) together with co-localized Raman spectroscopy. We show that the reduction is non-uniform leading to the coexistence of GO and rGO regions within the flakes, spanning a few hundred nanometers. By adjusting the reduction time, we can finely tune the ratio and degree of reduction of these specific regions. Furthermore, we demonstrate the effectiveness of monitoring the capacitance of the tip-sample system alongside local Raman spectroscopy data as a non-invasive and highly sensitive method to gain valuable insights into the nanoscale reduction process and its correlation with the local electronic properties.

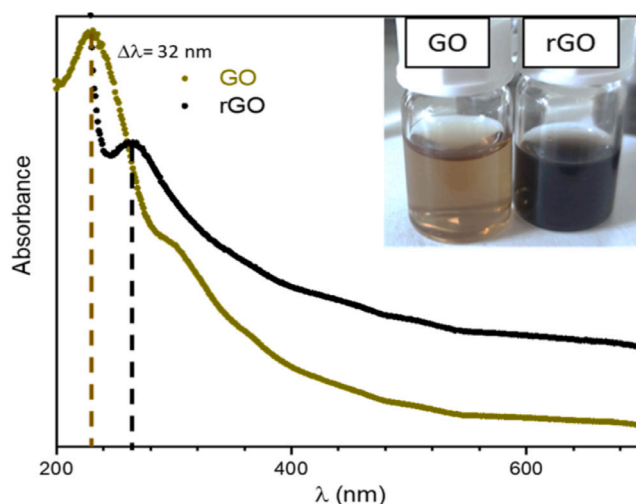


Fig. 1. UV-vis absorbance spectra for GO and rGO.

## 2. Experimental

### 2.1. Sample preparation

The samples were prepared on 300 nm SiO<sub>2</sub> thermally grown on highly doped p-type silicon (1–10 Ω cm, Siltronix) by drop-casting of ultradiluted (0.0004 wt%) GO and/or rGO solutions dispersed in Milli-Q type I water (MQ water). These dispersions yield low coverage and individual flakes. Prior to deposition, the substrate was rinsed with ethanol, MQ water and then exposed to UV/ozone for 15 min to remove organic contaminants and to ensure the hydrophilicity of the SiO<sub>2</sub> surface.

GO purchased from Graphenea was used without further treatment, while rGO with different reduction degrees was obtained from GO by using a simple one-pot surfactant-free chemical method at room temperature ( $T \approx 25$  °C). To start the reduction process, 0.05 mL of hydrazine hydrate (50 – 60%, Sigma Aldrich) was added to a 0.004 wt% 2 mL GO dispersion. After a certain reduction time, a small volume (200 μL) is extracted from the dispersion and further diluted to reach the final concentration. In order to achieve different reduction degrees, this process is repeated at increasing reduction times up to 4 days. After about 4 days, the original GO/hydrazine dispersion starts to agglomerate, indicating a high degree of reduction. Our partially reduced suspensions are stable for several weeks.

The reduction process can be visually confirmed through the change in color, from light brown to black, of the solution before and after reduction (Fig. 1). Additionally, the UV-vis absorbance spectra shows a redshift of the characteristic  $\pi - \pi^*$  absorption band from 230 to 262 nm for GO and rGO, respectively. This indicates that the conjugated structure is partially restored after the removal of some of the functional groups. In our case, we expect rGO which is not totally reduced as the maximum redshift reported with hydrazine reduction is found to be at 268 nm [32]. In addition, we are able to obtain stable rGO dispersions due to the low efficiency of hydrazine at removing hydroxyl and carboxyl groups that favors the stability, thanks to the electrostatic repulsion between the sheets. However, for increasing reduction time, the electrostatic repulsion diminishes and agglomeration of the sheets is observed [31]. Thus we expect rGO which is partially reduced and full of structural defects with no large extended  $sp^2$  domains since we have not performed an additional annealing process to restructure the carbon lattice [21].

An alternative procedure for chemical reduction with hydrazine consists on casting a droplet of hydrazine on top of already deposited GO samples. We have discarded this method however, as it worsened

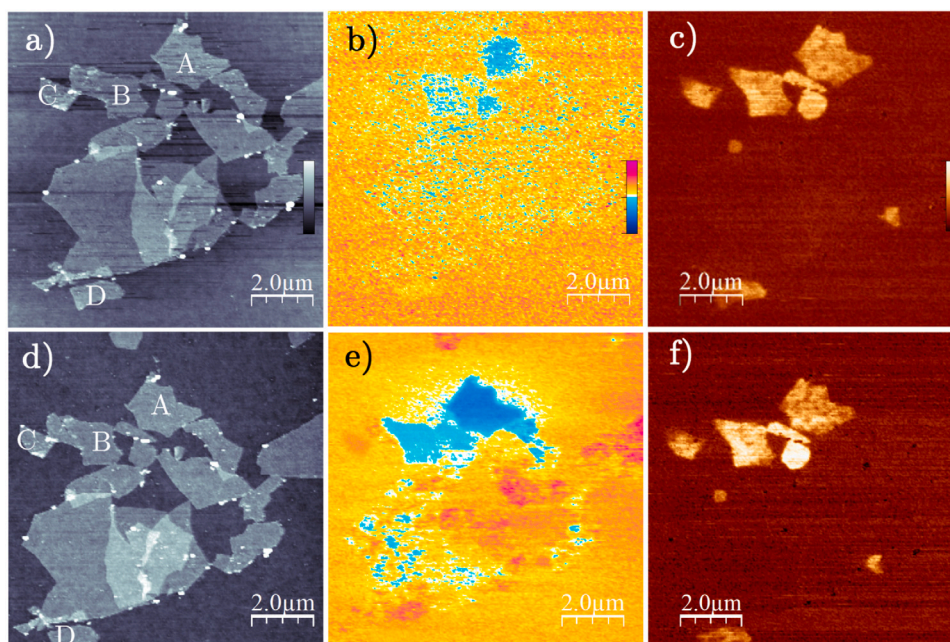


Fig. 2. Co-deposited GO and 16 h reduced rGO sample. (a)–(c) RH = 50%, (d)–(f) RH < 10%. (a) and (d) Topography (z scale 6 nm). (b) and (e) KPFM images (z scale 360 mV) and (c) and (f)  $2\omega_{\text{elec}}$  images.

our control over the experimental conditions. First of all, exposing the  $\text{SiO}_2$  surface to the hydrazine could modify it, introduce a higher variability in the properties of the measured flakes and make comparison between different experiments difficult and unreliable. Additionally, the small volume of the hydrazine droplet was very sensitive to changes in temperature and prone to evaporation, not allowing a good control of the reduction time.

## 2.2. Sample characterization

### 2.2.1. KPFM and $2\omega_{\text{elec}}$ signals

Topography and electrostatic measurements were performed as described in Ref. [47]. Using a dual lock-in Amplifier (Zurich instruments, HF2LI), two electrostatic signals can be measured simultaneously: (i) KPFM to obtain the sample's surface potential (SP); and (ii) the component oscillating at  $2\omega_{\text{elec}}$  which is related to the capacitance of the system formed by the tip and the sample through the following relation [48]

$$2\omega_{\text{elec}} \propto C(z)^{(n)} \cos(2\omega_{\text{elec}}t). \quad (1)$$

With  $C(z)^{(n)}$  being the  $n$ th derivative of the tip-sample capacitance,  $n = 1, 2$  when using the force (AM-KPFM) or the force gradient (FM-KPFM) as feedback, respectively. Thus, this signal is used to gain insight about the local tip-sample capacitance, which is closely related with the relative permittivity of the sample and, consequently, with its ability to screen electrical fields. All measurements were performed at controlled relative humidity (RH) in a  $\text{N}_2$  atmosphere.

### 2.2.2. Colocalized KPFM-Raman measurements

Colocalized KPFM-Raman scattering maps have been carried out with a Jobin-Yvon Xplora Raman confocal microscope attached to an AIST-NT AFM. The measurement procedure was as follows: a first scan over a square area was performed to record topography and SP of the samples with a lateral spatial step of around 20 nm; in a second scan over the same area Raman scattering was performed with a spatial step between 350 and 500 nm (typical Raman maps were  $40 \times 40$ ). Topography and SP maps were recorded in a two-pass mode, the first pass was done in tapping to get the topography and in the second one the tip was lifted an additional 30 nm over the sample and a 2 V

AC bias was applied to detect and cancel the electrostatic force. The noise fluctuations of the SP were below 5 mV. Raman spectra were acquired in backscattering configuration with a  $100\times$  objective, using the 600 groove/mm diffraction grating in a spectral range from 200 to  $5000 \text{ cm}^{-1}$ . We used a 532 nm laser diode with an excitation power of  $20 \text{ kW/cm}^2$ . The accumulation time for each spectrum was 2 s. KPFM measurements were carried out at RH < 10%. Raman scattering measurements were insensitive to humidity.

## 3. Results and discussion

### 3.1. Characterization of GO and rGO with SFM techniques

The ability of the Scanning Force Microscopy (SFM) techniques to record several interaction signals simultaneously has allowed us to distinguish between GO and rGO flakes and to correlate the experimental data with their different chemical and electronic properties. First of all we characterize simultaneously the two materials in samples where GO and rGO are co-deposited in order to establish their fingerprints in the different SFM channels. This way, problems such as changes in the tip or the measurement conditions or variations in the substrate, are avoided (characterization of GO and rGO individual samples are shown in the SI.1, Fig. SI. 1). Fig. 2 shows the topography, KPFM and  $2\omega_{\text{elec}}$  images of the co-deposited sample at both RH = 50% and RH < 10%. Although the two types of flakes are indistinguishable by their topographic features (height  $\sim 1.5 \text{ nm}$ ), they are clearly different in the electrostatic images (KPFM and  $2\omega_{\text{elec}}$  channels). Their signatures depend strongly on RH, at RH  $\sim 50\%$  there is very little contrast between the flakes and the substrate in the KPFM image. This is explained by the screening effect of the physisorbed water molecules on the surface (Fig. 2(b)). Despite the low contrast, two different types of flakes are observed: while some flakes show no SP difference with respect to the  $\text{SiO}_2$  substrate, others present a slightly negative SP.

Only after the humidity is decreased, RH < 10%, GO and rGO are unambiguously distinguished (Fig. 2(e)). GO flakes contain characteristic SP domains due to the presence of localized charges [49]. These domains are not observed on the rGO flakes, instead they display a nearly uniform SP. The absence of charge domains in rGO flakes is consistent with their larger conductivity and more extended electron

**Table 1**

Measured SP with respect to the substrate at RH = 50% and RH &lt; 10%.

Flake	SP RH < 10% (mV)	SP 50% RH (mV)
A	-630	70
B	-260	-40
C	125	Within the noise
D	Within the noise	20

wavefunctions as a result of the removal of the oxygen functional groups, and consequent recovery of the local  $sp^2$  hybridization [50,51]. While the SP is uniform within a given rGO flake, a significant SP variability is found among different rGO flakes. Table 1 summarizes the SP of the rGO flakes labeled in Figs. 2(a) and (d). For example, the rGO flake at the bottom (labeled D) has mostly the same SP as the substrate, while the rGO flakes located at the top (labeled A, B and C) have a non-zero SP. Moreover, rGO flakes touching each other share the same SP, which indicates a good electrical contact. On the contrary, rGO flakes separated by a GO sheet (B and C) show a different SP highlighting the insulating nature of GO. Since the flakes are supported on an insulating substrate, they lack a well-defined potential reference and thus their amount of charge, and therefore their SP, is affected by their local environment. Moreover, rGO flakes can be easily charged or discharged, which can happen through unintentional tip-sample contact during scanning (e.g., flake A). Nevertheless, although the regions of constant SP indicate the conducting nature of rGO, the measurement of the SP does not provide information about the degree of reduction of these flakes.

Moving on to the  $2\omega_{\text{elec}}$  images (Fig. 2(c) and (f)) the phenomenology is quite different: while GO flakes are not differentiated from the substrate [49], all the rGO flakes show a large signal and are clearly distinguishable, independently of the RH. This signal has been previously used to characterize a wide variety of systems, such as different human cells [52], subsurface features of different systems [53,54] or to explore the dielectric properties of different materials at the nanoscale [55,56]. The origin of the contrast is attributed to an increase in the tip-sample capacitance, however, the contributions to this signal vary depending on the system under study. The origin of the increased contrast over the rGO flakes will be discussed in more detail below, but it is clear that the local tip-sample capacitance is higher on the rGO flakes than on the GO flakes. Therefore, the  $2\omega_{\text{elec}}$  signal is sensitive to the reduction degree of the flakes and can even resolve substructures inside individual flakes.

Further information is obtained by injecting charge in GO and rGO at RH < 10% (Fig. 3). In these experiments, while measuring in non-contact mode, the tip is brought into contact at a given point and a bias voltage (typically 4 – 6 V) is applied between tip and sample for a short period of time (35 ms) [57]. Then, we continue the  $x-y$  scanning to monitor the evolution of the injected charge. A clearly different behavior is found between the two types of flakes. In GO (Fig. 3(a) and (b)), the injected charge spreads throughout the flake slowly enough to monitor it. On the contrary, Figs. 3(c) and (d) show how the charge distributes quickly over the whole flake when locally applying the bias to a rGO flake, confirming their improved in-plane conductivity as compared to that of GO. In fact, groups of flakes spanning tens of microns are “instantaneously” charged (with respect to the acquisition time), adopting the same SP. This implies a good electrical contact between them (see SI, Fig. SI.2). Consecutive KPFM images acquired after charging show that rGO flakes remain charged for a long period of time, indicating that the charge loss through the  $\text{SiO}_2$  substrate is small [57].

### 3.2. Co-localized Raman scattering

Raman spectroscopy, with its chemical and structural sensitivity, provides complementary information on the composition and disorder

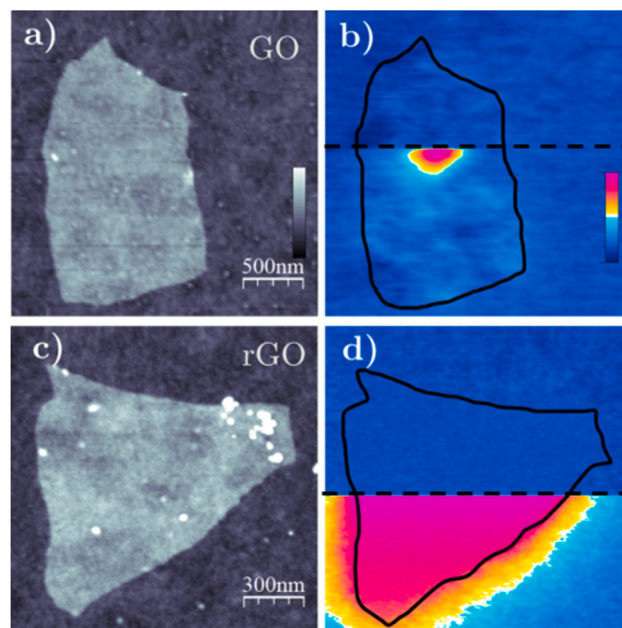
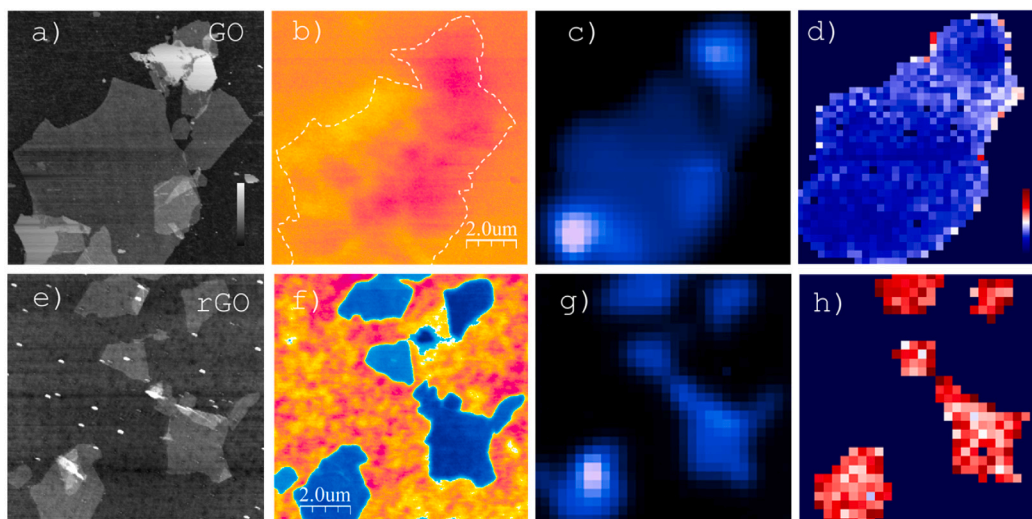


Fig. 3. Charge spreading in GO and rGO. (a) and (c) Topography ( $z$  scale = 4 nm), (b) and (d) KPFM images ( $z$  scale = 0 – 3 V) of the GO and rGO flakes during the charge injection experiments. The maps are recorded line by line from the top to the bottom of the image. A horizontal dashed line points the time of charge injection. The upper and lower sides of the images correspond to uncharged and charged flakes, respectively.

state of the GO flakes and thus could be a reliable metric for the reduction degree of the material. The Raman spectra of GO and rGO (see SI, Fig. SI.4) are almost identical at first sight. As stated in the introduction, an indepth quantitative analysis requires fitting the first-order Raman spectrum to five different peaks, namely:  $D^*$ ,  $D$ ,  $D'$ ,  $G$ , and  $D'$ . The most intense peaks are  $G$  ( $\sim 1585 \text{ cm}^{-1}$ ) and  $D$  ( $\sim 1350 \text{ cm}^{-1}$ ) and correspond to the  $E_{2g}$  optical phonon and a double resonant process mediated by disorder, respectively. The  $D''$  band ( $\sim 1520 \text{ cm}^{-1}$ ) arises from density of states and is related to the amorphous phase. The  $D'$  band ( $\sim 1620 \text{ cm}^{-1}$ ) has been attributed to an intra-valley resonance mediated by impurities. Finally, the  $D^*$  band ( $\sim 1150 \text{ cm}^{-1}$ ) is characteristic of  $sp^3$  phase and hexagonal diamond. In GO, this vibration is related to oxygen functional groups, such as hydroxyl groups, attached to the graphene plane. The implications of using different fitting function, whether Lorentzian, Gaussian or Voigt, to deconvolve the spectrum have been carefully analyzed (see SI.4). The data presented from now on has been obtained with three Lorentzian and two Gaussian functions.

We have recorded co-localized Raman scattering and KPFM maps of GO and rGO flakes dispersed on  $\text{SiO}_2$  substrates. Fig. 4 shows the results corresponding to topography, (a) and (e), SP, (b) and (f), integrated Raman intensity, (c) and (g), and  $I_{D^*}/I_G$  ratio, (d) and (h) for two samples consisting of GO and rGO, respectively.

In agreement with the findings of the previous section, GO and rGO flakes present substantial differences in their SP values when measured at RH < 10%. Concerning Raman scattering, several spectral features have been explored. The most reliable one is the intensity ratio of the  $D^*$  and  $G$  peaks ( $I_{D^*}/I_G$ ) for which a consistent increase is observed when comparing GO and rGO flakes: the average ratio is 0.072 for GO (Fig. 4(d)) and 0.145 for rGO flakes resulting from 48 h chemical reduction (Fig. 4(h)). Our results corroborate the relationship between the C/O ratio and  $I_{D^*}/I_G$  observed by Young Lee et al. [27] for thermally reduced rGO and provide an additional confirmation about the origin of the  $D^*$  band and its dependence on oxygen-containing groups.



**Fig. 4.** Co-localized KPFM-Raman scattering maps corresponding to GO and rGO flakes. For GO: (a) topography; (b) SP; (c) integrated Raman intensity; (d)  $I_{D^*}/I_G$  ratio. For rGO: (e) topography; (f) SP; (g) integrated Raman intensity; (h)  $I_{D^*}/I_G$  ratio. z scales are: 10 nm for topography; 200 mV for SP; 12 000 arbitrary units for Raman intensity; and 0.2 for  $D^*/G$  intensity ratio.

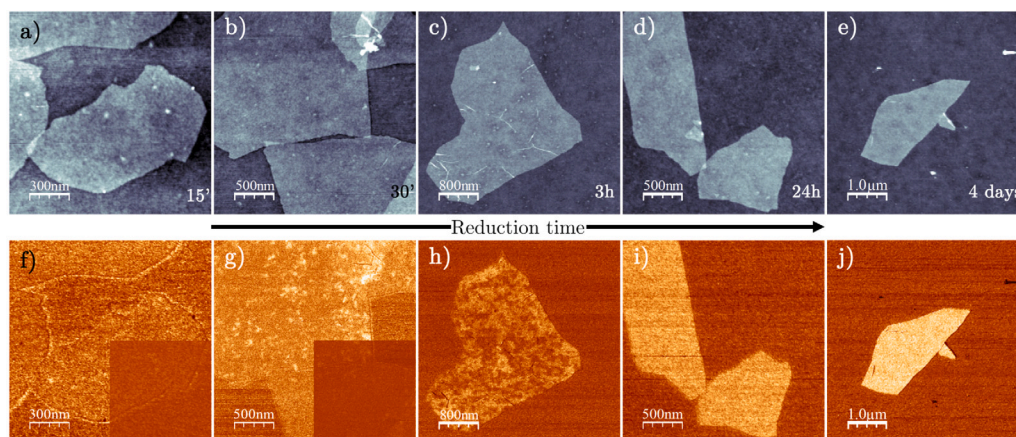


**Fig. 5.** Flakes with varying degrees of reduction: (a)–(e) Topography (z scale 4 nm) and (f)–(j)  $2\omega_{\text{elec}}$  images. In (f) and (g) the color scale is magnified by 50% to enhance the contrast of small signal shifts (bottom-right corner shows the color scale as in (h), (i) and (j)).

### 3.3. Intermediate reduction states: formation of GO/rGO hybrid flakes

The results presented above demonstrate that, although GO and rGO possess very different electronic properties, not all signals are suitable for identifying the different types of flakes or to evaluate the nanoscale reduction state. While topography and SP show no consistent differences and can be highly dependent on the experimental conditions,  $2\omega_{\text{elec}}$  and Raman scattering reveal a different picture for GO and rGO, independently of RH values or charge state. In order to explore the capabilities of these techniques, we have tracked the reduction of the GO sheets by monitoring the evolution of the  $2\omega_{\text{elec}}$  signal and the  $I_{D^*}/I_G$  ratio as a function of the reduction time. Samples with varying degrees of reduction (ranging from 15 min to 4 days) were prepared following the procedure detailed in the experimental section. As in any AFM related technique, the reliability of the results obtained from the  $2\omega_{\text{elec}}$  signal depends on the stability of various parameters during the experiment, such as the tip's radius and composition, the tip-sample distance or the RH, among others. For this reason, we have established a rigorous measurement protocol, which is explained in SI. 8

The evolution of the  $2\omega_{\text{elec}}$  signal is shown in Fig. 5. In the first stages of the reduction process, small bright randomly distributed spots appear over the GO sheets (Fig. 5(f)). As the reduction process goes on, the amount, size, and contrast of these spots increases, forming small domains (Fig. 5(g)). These regions keep growing in size until they merge, forming extended domains with a lateral size between 30 and 400 nm that percolate through the flakes (Fig. 5(h)). Darker domains are regions with a lower degree of reduction. As the reduction process carries on, these structures extend over the flake until it becomes roughly homogeneous (Fig. 5(i)). The flakes can be further reduced, increasing the overall contrast of the  $2\omega_{\text{elec}}$  signal (Fig. 5(j)). A detailed inspection reveals that these flakes are not completely homogeneous but, even at this reduction stage, there are still regions with different degrees of reduction (see SI, Fig. SI. 3). We recall that, as mentioned in the experimental section, with the reduction method employed here we do not achieve a complete reduction.

Based on our results, it is evident that an increase in the reduction degree leads a corresponding increase in the  $2\omega_{\text{elec}}$  signal. This suggests that higher reduced regions are able to screen the electric fields within

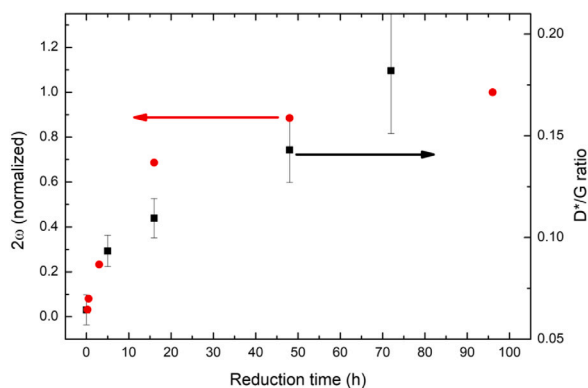


**Fig. 6.** Normalized  $2\omega_{\text{elec}}$  value and  $I_{D^*}/I_G$  displayed as a function of the reduction time of rGO flakes.

the tip-sample capacitor more efficiently. These results are in line with our expectations for a material displaying a more pronounced metallic behavior. Consequently, this signal proves to be highly suitable for evaluating the local degree of reduction, owing to its sensitivity and lateral resolution that allows for the differentiation of distinct regions within a single flake. However, a quantitative interpretation of the  $2\omega_{\text{elec}}$  signal is still lacking. Even at a theoretical level, the study of the electrostatic screening of two-dimensional nanomaterials represents a major challenge. In particular, the screening of the electric field generated by a point charge located at a distance  $z$  on top of a 2D material has been studied when it is measured below the material [58]. The response of the system depends on many parameters: charge distance, local polarizability, surface conductivity and in a non trivial way on band structure, density response nonlocality, strain or number of layers.

Although there are several contributions to the  $2\omega_{\text{elec}}$  signal, in the context of SFM, the tip-sample distance can be maintained constant, and it is reasonable to assume that the rest of variables will have a monotonic variation as a function of the degree of reduction. This opens up the possibility of using it for a quantitative estimation of the average degree of reduction. To confirm it, we compare the evolution of the  $I_{D^*}/I_G$  peaks ratio from colocalized Raman spectra as a function of the reduction time, with the corresponding average value of the  $2\omega_{\text{elec}}$  signal across multiple flakes at a given reduction time (Fig. 6). As the units of this signal are arbitrary, we have normalized the values by dividing them by the maximum measured value. Consequently, the signal ranges from 0 to 1, with 0 corresponding to GO and 1 to our most reduced flakes respectively. As previously argued, the evolution of this signal exhibits a clearly increasing trend as a function of the reduction time which completely aligns with the trend of the  $I_{D^*}/I_G$  ratio, hence

confirming its value as an estimator of the degree of reduction and its correlation with the C/O ratio.

Finally, the electrical properties of the different regions observed in the partially reduced flakes have been investigated. We study how injected charge is distributed within the different zones and how it correlates with the  $2\omega_{\text{elec}}$  signal (Fig. 7). Before charging, the SP image shows little contrast and different regions are nearly indistinguishable (Fig. 7(b)). After positive (negative) charge injection, the whole flake becomes “instantaneously” positively (negatively) charged (Fig. 7(c) and (d)), respectively. The brighter (more reduced) regions in the  $2\omega_{\text{elec}}$  image (Fig. 7(a)) tend to concentrate more charge, independently of the sign of the injected charge. This confirms a more metal-like character of the bright regions, which is the cause of the increased contrast of the SP image and the correlation (anti-correlation) that arises between the SP and the  $2\omega_{\text{elec}}$  images after charging. This proves that ‘hybrid’ partially reduced flakes exhibit different local properties, and opens up the possibility of using them as a template for selective functionalization.

#### 4. Conclusions

In summary, we have investigated the evolution of the nanoscale electronic properties of monolayer GO flakes as they undergo gradual transformation to rGO through hydrazine chemical reduction. We find that KPFM is a valuable technique for qualitatively assessing the increase in conductivity with the reduction degree, as observed through the SP maps and by monitoring the spread of the injected charge. However, we demonstrate that KPFM alone is not sufficient to fully characterize the reduction state, and complementary local techniques should be applied. In this regard, we show that the combined capabilities of co-localized KPFM-Raman measurements provide information that correlates the structure and composition of the flakes with their electronic properties, while the  $2\omega_{\text{elec}}$  signal grants remarkable sensitivity to the degree of reduction. Through the careful implementation of fitting routine of the Raman spectral features, we have successfully identified that the intensity ratio  $I_{D^*}/I_G$  consistently increases with the degree of reduction and provides a reliable metric for the degree of reduction. Furthermore, this trend exhibits a strong correlation with the evolution of the  $2\omega_{\text{elec}}$  signal as a function of the reduction time, which confirms the capability to identify the degree of reduction through  $2\omega_{\text{elec}}$  signal. Consequently, these two contactless techniques serve as suitable complements to KPFM, with the additional advantage of being less sensitive to the relative humidity than KPFM. Additionally, leveraging the excellent lateral resolution of the  $2\omega_{\text{elec}}$  signal, we show that different regions with different degree of reduction coexist within a single flake. Thus, we unveil a non-uniform reduction process in which domains with distinctly different properties are differentiated, providing individual sheets with the rich chemistry of GO and the increased conducting properties of rGO.

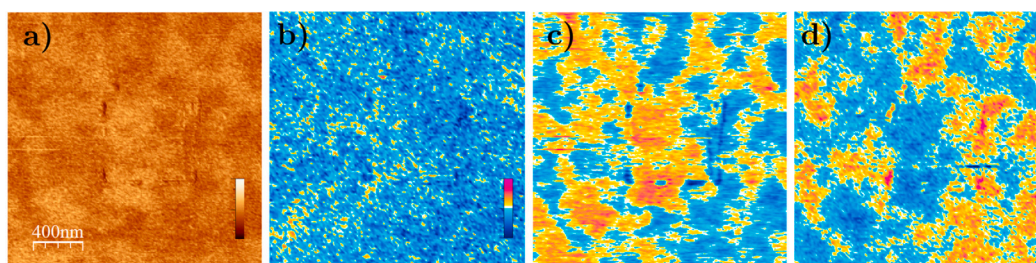


**Fig. 7.** (a)  $2\omega_{\text{elec}}$  (b) SP image of a partially reduced flake ( $z$  scale 200 mV). (c) SP image of a positively charged ( $z$  scale 660 mV). (d) SP image of a negatively charged, partially reduced flake ( $z$  scale 500 mV). The  $z$  scale has been adjusted around the mean SP value in each image.

## CRediT authorship contribution statement

**M. Navarro-Rodriguez:** Investigation, Data curation, Visualization, Writing – review & editing. **V. Camús:** Investigation, Formal analysis. **A. Cros:** Methodology, Writing – review & editing, Funding acquisition. **N. Garro:** Conceptualization, Methodology, Supervision, Writing – review & editing, Funding acquisition. **Andres M. Somoza:** Methodology, Formal analysis, Writing – review & editing. **E. Palacios-Lidon:** Conceptualization, Methodology, Supervision, Writing – original draft, Funding acquisition.

## Declaration of competing interest

The authors declare that they have no known competing financial interests or personal relationships that could have appeared to influence the work reported in this paper.

## Data availability

Data will be made available on request.

## Acknowledgments

The authors thank the funding agencies MCIN/AEI/10.13039/501100011033 through projects PID2019-104272RB-C52 and PID2019-104272RB-C53; “ERDF A way of making Europe”; and Generalitat Valenciana through project CIPROM-2021-75; and the Advanced Materials programme by MCIN with funding from European Union NextGenerationEU (PRTR-C17.11) and by Generalitat Valenciana (Grant MFA/2022/007). M.N work was financed by the grant PID2019-104272RB-C52/PRE2020-094503 funded by MCIN/AEI/10.13039/501100011033 and by “ESF Investing in your future”.

## Appendix A. Supplementary data

Supplementary material related to this article can be found online at <https://doi.org/10.1016/j.apsusc.2023.158611>.

## References

- [1] D.R. Dreyer, S. Park, C.W. Bielawski, R.S. Ruoff, The chemistry of graphene oxide, *Chem. Soc. Rev.* 39 (1) (2010) 228–240, <http://dx.doi.org/10.1039/B917103G>.
- [2] Z. Liu, K. Nørgaard, M.H. Overgaard, M. Ceccato, D.M.A. Mackenzie, N. Stenger, S.L.S. Stipp, T. Hassenkam, Direct observation of oxygen configuration on individual graphene oxide sheets, *Carbon* 127 (2018) 141–148, <http://dx.doi.org/10.1016/j.carbon.2017.10.100>.
- [3] F. Mouhat, F.-X. Coudert, M.-L. Bocquet, Structure and chemistry of graphene oxide in liquid water from first principles, *Nature Commun.* 11 (1) (2020) 1566, <http://dx.doi.org/10.1038/s41467-020-15381-y>.
- [4] W.S.J. Hummers, R.E. Offeman, Preparation of graphitic oxide, *J. Am. Chem. Soc.* 80 (6) (1958) 1339, <http://dx.doi.org/10.1021/ja01539a017>.
- [5] D.C. Marcano, D.V. Kosynkin, J.M. Berlin, A. Sinitskii, Z. Sun, A. Slesarev, L.B. Alemany, W. Lu, J.M. Tour, Improved synthesis of graphene oxide, *ACS Nano* 4 (8) (2010) 4806–4814, <http://dx.doi.org/10.1021/nn1006368>.
- [6] L. Shahriari, A.A. Athawale, Graphene oxide synthesized by using modified hummers approach, *Int. J. Renew. Energy Environ. Eng.* 2 (1) (2014) 58–63.
- [7] B.C. Brodie, XIII. On the atomic weight of graphite, *Philos. Trans. R. Soc. Lond.* 149 (1859) 249–259, <http://dx.doi.org/10.1098/rstl.1859.0013>.
- [8] A. Jiříčková, O. Jankovský, Z. Sofer, D. Sedmidubský, Synthesis and applications of graphene oxide, *Materials* 15 (3) (2022) 920, <http://dx.doi.org/10.3390/ma15030920>.
- [9] X.-M. Huang, L.-Z. Liu, S. Zhou, J.-J. Zhao, Physical properties and device applications of graphene oxide, *Front. Phys.* 15 (3) (2020) 33301, <http://dx.doi.org/10.1007/s11467-019-0937-9>.
- [10] S. Porro, E. Accornero, C.F. Pirri, C. Ricciardi, Memristive devices based on graphene oxide, *Carbon* 85 (2015) 383–396, <http://dx.doi.org/10.1016/j.carbon.2015.01.011>.
- [11] K. Fu, Y. Wang, C. Yan, Y. Yao, Y. Chen, J. Dai, S. Lacey, Y. Wang, J. Wan, T. Li, Z. Wang, Y. Xu, L. Hu, Graphene oxide-based electrode inks for 3D-printed lithium-ion batteries, *Adv. Mater.* 28 (13) (2016) 2587–2594, <http://dx.doi.org/10.1002/adma.201505391>.
- [12] K. Krishnamoorthy, R. Mohan, S.-J. Kim, Graphene oxide as a photocatalytic material, *Appl. Phys. Lett.* 98 (24) (2011) 244101, <http://dx.doi.org/10.1063/1.3599453>.
- [13] J. Pyun, Graphene oxide as catalyst: Application of carbon materials beyond nanotechnology, *Angew. Chem. Int. Ed.* 50 (1) (2011) 46–48, <http://dx.doi.org/10.1002/anie.2011003897>.
- [14] Q. Gu, G. Wen, Y. Ding, K.-H. Wu, C. Chen, D. Su, Reduced graphene oxide: a metal-free catalyst for aerobic oxidative desulfurization, *Green Chem.* 19 (4) (2017) 1175–1181, <http://dx.doi.org/10.1039/C6GC02894B>, Publisher: The Royal Society of Chemistry.
- [15] S. Borini, R. White, D. Wei, M. Astley, S. Haque, E. Spigone, N. Harris, J. Kivioja, T. Ryhänen, Ultrafast graphene oxide humidity sensors, *ACS Nano* 7 (12) (2013) 11166–11173, <http://dx.doi.org/10.1021/nn404889b>.
- [16] D. Lei, Q. Zhang, N. Liu, T. Su, L. Wang, Z. Ren, Z. Zhang, J. Su, Y. Gao, Self-powered graphene oxide humidity sensor based on potentiometric humidity transduction mechanism, *Adv. Funct. Mater.* 32 (10) (2022) 2107330, <http://dx.doi.org/10.1002/adfm.202107330>.
- [17] A.M.L. Oliveira, M. Machado, G.A. Silva, D.B. Bitoque, J. Tavares Ferreira, L.A. Pinto, Q. Ferreira, Graphene oxide thin films with drug delivery function, *Nanomaterials* 12 (7) (2022) 1149, <http://dx.doi.org/10.3390/nano12071149>.
- [18] H. Huang, S. Su, N. Wu, H. Wan, S. Wan, H. Bi, L. Sun, Graphene-based sensors for human health monitoring, *Front. Chem.* 7 (2019).
- [19] W. Liu, X. Zhang, L. Zhou, L. Shang, Z. Su, Reduced graphene oxide (rGO) hybridized hydrogel as a near-infrared (NIR)/pH dual-responsive platform for combined chemo-photothermal therapy, *J. Colloid Interface Sci.* 536 (2019) 160–170, <http://dx.doi.org/10.1016/j.jcis.2018.10.050>.
- [20] Y. Wei, Y. Zhang, X. Gao, Z. Ma, X. Wang, C. Gao, Multilayered graphene oxide membranes for water treatment: A review, *Carbon* 139 (2018) 964–981, <http://dx.doi.org/10.1016/j.carbon.2018.07.040>.
- [21] K. Krishnamoorthy, M. Veerapandian, K. Yun, S.J. Kim, The chemical and structural analysis of graphene oxide with different degrees of oxidation, *Carbon* 53 (2013) 38–49, <http://dx.doi.org/10.1016/j.carbon.2012.10.013>.
- [22] Y. Chen, K. Fu, S. Zhu, W. Luo, Y. Wang, Y. Li, E. Hitz, Y. Yao, J. Dai, J. Wan, V.A. Danner, T. Li, L. Hu, Reduced graphene oxide films with ultrahigh conductivity as Li-ion battery current collectors, 2016, <http://dx.doi.org/10.1021/acs.nanolett.6b00743>.
- [23] Y. Wang, Y. Chen, S.D. Lacey, L. Xu, H. Xie, T. Li, V.A. Danner, L. Hu, Reduced graphene oxide film with record-high conductivity and mobility, *Mater. Today* 21 (2) (2018) 186–192, <http://dx.doi.org/10.1016/j.mattod.2017.10.008>.
- [24] S. Pei, H.-M. Cheng, The reduction of graphene oxide, *Carbon* 50 (9) (2012) 3210–3228, <http://dx.doi.org/10.1016/j.carbon.2011.11.010>.
- [25] A.A.K. King, B.R. Davies, N. Noorbehesht, P. Newman, T.L. Church, A.T. Harris, J.M. Razal, A.I. Minett, A new Raman metric for the characterisation of graphene oxide and its derivatives, *Sci. Rep.* 6 (1) (2016) 19491, <http://dx.doi.org/10.1038/srep19491>.
- [26] S. Claramunt, A. Varea, D. López-Díaz, M.M. Velázquez, A. Cornet, A. Cirera, The importance of interbands on the interpretation of the Raman spectrum of graphene oxide, *J. Phys. Chem. C* 119 (18) (2015) 10123–10129, <http://dx.doi.org/10.1021/acs.jpcc.5b01590>.
- [27] A.Y. Lee, K. Yang, N.D. Anh, C. Park, S.M. Lee, T.G. Lee, M.S. Jeong, Raman study of D\* band in graphene oxide and its correlation with reduction, *Appl. Surf. Sci.* 536 (2021) 147990, <http://dx.doi.org/10.1016/j.apsusc.2020.147990>.
- [28] B. Ma, R.D. Rodriguez, A. Ruban, S. Pavlov, E. Sheremet, The correlation between electrical conductivity and second-order Raman modes of laser-reduced graphene oxide, *Phys. Chem. Chem. Phys.* 21 (19) (2019) 10125–10134, <http://dx.doi.org/10.1039/C9CP00093C>.
- [29] K.K.H. De Silva, P. Viswanath, V.K. Rao, S. Suzuki, M. Yoshimura, New insight into the characterization of graphene oxide and reduced graphene oxide monolayer flakes on Si-based substrates by optical microscopy and Raman spectroscopy, *J. Phys. Chem. C* 125 (14) (2021) 7791–7798, <http://dx.doi.org/10.1021/acs.jpcc.1c01152>.
- [30] S. Eigler, A.M. Dimiev, Functionalization and reduction of graphene oxide, in: *Graphene Oxide*, John Wiley & Sons, Ltd, 2016, pp. 175–229, <http://dx.doi.org/10.1002/9781119069447.ch6>, Ch. 6.
- [31] V. Agarwal, P.B. Zetterlund, Strategies for reduction of graphene oxide – A comprehensive review, *Chem. Eng. J.* 405 (2021) 127018, <http://dx.doi.org/10.1016/j.cej.2020.127018>.
- [32] M.J. Fernández-Merino, L. Guardia, J.I. Paredes, S. Villar-Rodil, P. Solís-Fernández, A. Martínez-Alonso, J.M.D. Tascón, Vitamin C is an ideal substitute for hydrazine in the reduction of graphene oxide suspensions, *J. Phys. Chem. C* 114 (14) (2010) 6426–6432, <http://dx.doi.org/10.1021/jp100603h>.
- [33] S. Park, J. An, J.R. Potts, A. Velamakanni, S. Murali, R.S. Ruoff, Hydrazine-reduction of graphite- and graphene oxide, *Carbon* 49 (9) (2011) 3019–3023, <http://dx.doi.org/10.1016/j.carbon.2011.02.071>.
- [34] M. Pelaez-Fernandez, A. Bermejo, A.M. Benito, W.K. Maser, R. Arenal, Detailed thermal reduction analyses of graphene oxide via in-situ TEM/EELS studies, *Carbon* 178 (2021) 477–487, <http://dx.doi.org/10.1016/j.carbon.2021.03.018>.

- [35] M.A. Cenicerós-Reyes, K.S. Marín-Hernández, U. Sierra, E.M. Saucedo-Salazar, R. Mendoza-Resendez, C. Luna, P.J. Hernández-Belmares, O.S. Rodríguez-Fernández, S. Fernández-Tavizón, E. Hernández-Hernández, E.D. Barriga-Castro, Reduction of graphene oxide by in-situ heating experiments in the transmission electron microscope, *Surf. Interfaces* 35 (2022) 102448, <http://dx.doi.org/10.1016/j.surfint.2022.102448>.
- [36] S. Hettler, D. Sebastian, M. Pelaez-Fernandez, A.M. Benito, W.K. Maser, R. Arenal, In-situ reduction by Joule heating and measurement of electrical conductivity of graphene oxide in a transmission electron microscope, *2D Mater.* 8 (3) (2021) 031001, <http://dx.doi.org/10.1088/2053-1583/abcd9>.
- [37] Z. Wei, D. Wang, S. Kim, S.-Y. Kim, Y. Hu, M.K. Yakes, A.R. Laracuente, Z. Dai, S.R. Marder, C. Berger, W.P. King, W.A. de Heer, P.E. Sheehan, E. Riedo, Nanoscale tunable reduction of graphene oxide for graphene electronics, *Science* 328 (5984) (2010) 1373–1376, <http://dx.doi.org/10.1126/science.1188119>.
- [38] A.C. Faucett, J.M. Mativetsky, Nanoscale reduction of graphene oxide under ambient conditions, *Carbon* 95 (2015) 1069–1075, <http://dx.doi.org/10.1016/j.carbon.2015.09.025>.
- [39] S. Zhu, J. Zeng, S. Zhang, W. Song, Y. Sun, X. Ren, X. Li, C. Hai, Y. Shen, Effects of graphene redox on its triboelectrification at the nanoscale, *J. Phys. Chem. C* 126 (46) (2022) 19559–19570, <http://dx.doi.org/10.1021/acs.jpcc.2c03170>.
- [40] D.D. Kulkarni, S. Kim, M. Chyasnachyus, K. Hu, A.G. Fedorov, V.V. Tsukruk, Chemical reduction of individual graphene oxide sheets as revealed by electrostatic force microscopy, *J. Am. Chem. Soc.* 136 (18) (2014) 6546–6549, <http://dx.doi.org/10.1021/ja5005416>.
- [41] Y. Shen, Y. Wang, J. Zhang, C. Hai, Y. Zhou, J. Hu, Y. Zhang, Sample-charged mode scanning polarization force microscopy for characterizing reduced graphene oxide sheets, *J. Appl. Phys.* 115 (24) (2014) 244302, <http://dx.doi.org/10.1063/1.4883538>.
- [42] Y. Shen, S. Zhang, Y. Sun, C. Hai, X. Li, J. Zeng, X. Ren, Z. Yuan, Structure and properties evolution of graphene oxide sheets during low-temperature reduction on a solid substrate, *J. Phys. Chem. C* XXXX (2020) <http://dx.doi.org/10.1021/acs.jpcc.0c03499>.
- [43] Y. Shen, Y. Wang, Y. Zhou, C. Hai, J. Hu, Y. Zhang, Electrostatic force spectroscopy revealing the degree of reduction of individual graphene oxide sheets, *Beilstein J. Nanotechnol.* 9 (2018) 1146–1155, <http://dx.doi.org/10.3762/bjnano.9.106>.
- [44] J.B. Kim, S.H. Koo, I.H. Kim, J.T. Kim, J.G. Kim, B. Jayaraman, J. Lim, S.O. Kim, Characteristic dual-domain composite structure of reduced graphene oxide and its application to higher specific capacitance, *Chem. Eng. J.* 446 (2022) 137390, <http://dx.doi.org/10.1016/j.cej.2022.137390>.
- [45] R. Negishi, K. Takashima, Y. Kobayashi, Investigation of surface potentials in reduced graphene oxide flake by Kelvin probe force microscopy, *Japan. J. Appl. Phys.* 57 (6S1) (2018) 06HD02, <http://dx.doi.org/10.7567/JJAP.57.06HD02>.
- [46] O.M. Slobodian, P.M. Lytvyn, A.S. Nikolenko, V.M. Naseka, O.Y. Khyzhun, A.V. Vasin, S.V. Sevostianov, A.N. Nazarov, Low-temperature reduction of graphene oxide: Electrical conductance and scanning kelvin probe force microscopy, *Nanoscale Res. Lett.* 13 (1) (2018) 139, <http://dx.doi.org/10.1186/s11671-018-2536-z>.
- [47] E. Palacios-Lidón, B. Pérez-García, J. Colchero, Enhancing dynamic scanning force microscopy in air: as close as possible, *Nanotechnology* 20 (8) (2009) 085707, <http://dx.doi.org/10.1088/0957-4484/20/8/085707>.
- [48] S. Sadewasser, T. Glatzel, *Kelvin Probe Force Microscopy: From Single Charge Detection to Device Characterization*, Springer, 2018.
- [49] E. Palacios-Lidón, J. Colchero, M. Ortuno, E. Colom, A.M. Benito, W.K. Maser, A.M. Somoza, Nanoscale charge density and dynamics in graphene oxide, *ACS Mater. Lett.* 3 (12) (2021) 1826–1831, <http://dx.doi.org/10.1021/acsmaterialslett.1c00550>.
- [50] D. Joung, S.I. Khondaker, Efros-Shklovskii variable-range hopping in reduced graphene oxide sheets of varying carbon  $sp^2$  fraction, *Phys. Rev. B* 86 (23) (2012) 235423, <http://dx.doi.org/10.1103/PhysRevB.86.235423>.
- [51] R. Cheruku, D.S. Bhaskaram, G. Govindaraj, Variable range hopping and relaxation mechanism in graphene oxide sheets containing  $Sp^3$  hybridization induced localization, *J. Mater. Sci.: Mater. Electron.* 29 (11) (2018) 9663–9672, <http://dx.doi.org/10.1007/s10854-018-9003-6>.
- [52] W. Zhao, W. Cui, S. Xu, L.-Z. Cheong, D. Wang, C. Shen, Direct study of the electrical properties of PC12 cells and hippocampal neurons by EFM and KPFM, *Nanoscale Adv.* 1 (2) (2019) 537–545, <http://dx.doi.org/10.1039/C8NA00202A>.
- [53] M.J. Cadena, S.H. Sung, B.W. Boudouris, R. Reifengerger, A. Raman, Nanoscale mapping of dielectric properties of nanomaterials from kilohertz to megahertz using ultrasmall cantilevers, *ACS Nano* 10 (4) (2016) 4062–4071, <http://dx.doi.org/10.1021/acsnano.5b06893>.
- [54] O.A. Castañeda-Urbe, R. Reifengerger, A. Raman, A. Avila, Depth-sensitive subsurface imaging of polymer nanocomposites using second harmonic kelvin probe force microscopy, *ACS Nano* 9 (3) (2015) 2938–2947, <http://dx.doi.org/10.1021/nn507019c>.
- [55] M.J. Cadena, R.G. Reifengerger, A. Raman, High resolution subsurface imaging using resonance-enhanced detection in 2nd-harmonic KPFM, *Nanotechnology* 29 (40) (2018) 405702, <http://dx.doi.org/10.1088/1361-6528/aacfdc>.
- [56] D. Jeon, Y. Kang, T. Kim, Correlation between the dielectric response and thickness of vanadium pentoxide nanowires, *ACS Appl. Electron. Mater.* 4 (1) (2022) 124–129, <http://dx.doi.org/10.1021/acsaelm.1c00733>.
- [57] M. Navarro-Rodríguez, E. Palacios-Lidón, A.M. Somoza, The surface charge decay: A theoretical and experimental analysis, *Appl. Surf. Sci.* 610 (2023) 155437, <http://dx.doi.org/10.1016/j.apsusc.2022.155437>.
- [58] A. Ambrosetti, P.L. Silvestrelli, Faraday-like screening by two-dimensional nanomaterials: A scale-dependent tunable effect, *J. Phys. Chem. Lett.* 10 (9) (2019) 2044–2050.